PHOTONICS Research

Highly stable full-color display device with VLC application potential using semipolar μLEDs and all-inorganic encapsulated perovskite nanocrystal

Tingzhu Wu,[1,2,†] Yue Lin,[1,2,†] Yu-Ming Huang,[3,†] Meng Liu,[1] Konthoujam James Singh,[3] Wansheng Lin,[1] Tingwei Lu,[1] Xi Zheng,[1] Jianyang Zhou,[1] Hao-Chung Kuo,[3,4,5] and Zhong Chen[1,2,6]

[1]School of Electronic Science and Engineering, Fujian Engineering Research Center for Solid-State Lighting, Xiamen University, Xiamen 361005, China
[2]Fujian Science & Technology Innovation Laboratory for Energy Materials of China, Xiamen 361005, China
[3]Department of Photonics and Graduate Institute of Electro-Optical Engineering, College of Electrical and Computer Engineering, Taiwan Chiao Tung University, Hsinchu 30010, China
[4]Semiconductor Research Center, Hon Hai Research Institute, Taipei 11492, China
[5]e-mail: hckuo@faculty.nctu.edu.tw
[6]e-mail: chenz@xmu.edu.cn

Received 10 May 2021; revised 23 August 2021; accepted 24 August 2021; posted 24 August 2021 (Doc. ID 431095); published 6 October 2021

A promising approach for the development of effective full-color displays is to combine blue microLEDs (μLEDs) with color conversion layers. Perovskite nanocrystals (PNCs) are notable for their tolerance to defects and provide excellent photoluminescence quantum yields and high color purity compared to metal chalcogenide quantum dots. The stability of PNCs in ambient conditions and under exposure to blue light can be improved using a SiO_2 coating. This study proposes a device that could be used for both display and visible light communication (VLC) applications. The semipolar blue μLED array fabricated in this study shows a negligible wavelength shift, indicating a significant reduction in the quantum confined Stark effect. Owing to its shorter carrier lifetime, the semipolar μLED array exhibits an impressive peak 3 dB bandwidth of 655 MHz and a data transmission rate of 1.2 Gb/s corresponding to an injection current of 200 mA. The PNC–μLED device assembled from a semipolar μLED array with PNCs demonstrates high color stability and wide color-gamut features, achieving 127.23% and 95.00% of the National Television Standards Committee standard and Rec. 2020 on the CIE 1931 color diagram, respectively. These results suggest that the proposed PNC–μLED device is suitable for both display-related and VLC applications.

https://doi.org/10.1364/PRJ.431095

1. INTRODUCTION

Owing to their versatility and tunability, microLEDs (μLEDs) with sizes less than 50 μm are considered integral components of next-generation display technology and are able to satisfy the demands of sophisticated devices, such as cellphones, smart watches, virtual reality, microprojectors, and ultra-high-definition TVs [1,2]. Over the past decade, the number of commercially available μLED displays has grown significantly, as manufacturers seek to capitalize on the success of this technology [3]. μLEDs have the potential to surpass organic LEDs by providing displays with high contrast, a wide color gamut, high efficiency, and a wide viewing angle, which are additional to the prospect of translucent and versatile displays [4]. Huang Chen *et al.* demonstrated a hybrid quantum dot–nanoring–μLED that exhibited a color gamut of approximately 104.8% of the National Television Standards Committee (NTSC) standard and 78.2% of Rec. 2020 [4,5]. Huang *et al.* achieved a record high external quantum efficiency (EQE) for green and blue QLEDs, and the devices exhibited a record 90% coverage of Rec. 2020, which exhibits lifetimes longer than 100,000 and 280,000 h for green and red QLEDs for ultra-high definition displays, respectively [5]. Full-color displays can be achieved via mass transfer processes using RGB μLEDs. However, this approach has several drawbacks, such as low efficiency caused by the so-called "green-gap" originating from green μLEDs and nonradiative recombination at the surface for red μLEDs owing to the use of AlGaInP as the active region material [6]. A further problem for red μLEDs is that the EQE decreases when the pixel size decreases [7]. To address these problems, blue μLEDs can be integrated with color converters, such as yellow-emitting phosphors or nanocrystals (NCs) that emit red and green light, to achieve higher quality full-color displays [8]. Lin *et al.* successfully fabricated

high-luminance efficiency and a wide color gamut for an NC-based solid and hybrid-type WLED device, which exhibits a higher efficiency (51 lm/W), a wide color gamut (122% of NTSC and 91% of Rec. 2020), and an efficiency decay of approximately 12% during a 200 h reliability test [9]. However, phosphors are not suitable for microdisplay technology because of their large particle size [10]. In contrast, NCs offer several compelling features, including the quantum confinement effect (specifically for quantum dots), a narrow emission spectrum, high quantum yield, and low manufacturing costs, which makes them an attractive alternative for phosphors in full-color displays [11].

Perovskite NCs (PNCs), especially those that are lead-based, demonstrate significant advantages over conventional semiconductor NC systems, attracting extensive interest from researchers and manufacturers seeking to produce cost-effective and wide-color-gamut displays [12,13]. Nevertheless, PNCs have some drawbacks. They have, for example, exhibited vulnerability under ambient conditions, particularly in the case of red-emitting PNCs that contain iodine [14]. Water vapor, oxygen, high temperature, and light irradiation cause alteration to the crystal structures of PNCs, typically resulting in photoluminescence (PL) quenching [15]. Several approaches have been explored to enhance the stability of PNCs, among which the most straightforward one is to encapsulate the PNCs in polymer or inorganic shells, thereby preventing the infiltration of water vapor and oxygen [16]. However, polymers are also vulnerable under blue light irradiation, which is inevitable in display technologies [17]. To address this issue, all-inorganic silica encapsulation is adopted for both red and green PNCs in this work, resulting in excellent stability under ambient conditions and, specifically, in response to blue light irradiation.

Even if full-color displays are achieved, the stability of color performance still must be considered. Because of the quantum-confined Stark effect (QCSE), the emitting wavelength of the μLED can shift dramatically under different operating currents [18]. This color shift induced by QCSE is unfavored in display applications, such as mobile phones or laptops, which typically need to operate under different lighting conditions. The wavelength shift can be generated when adjusting the intensity of the display brightness, thereby affecting its color performance. To address these problems, the conventional c-plane μLED can be replaced with nonpolar or semipolar μLEDs that have less QSCE and can thereby achieve a smaller color shift [19]. Huang Chen *et al.* reported an RGB full-color semipolar μLED device, which has a wide color gamut of 114.4% of the NTSC and 85.4% of the Rec. 2020. The semipolar μ-LED exhibits a stabilizing wavelength shift of 3.2 nm compared to the c-plane μLED's shift of 13.0 nm [20].

In addition to displays, μLEDs have recently been adopted as transmitters in visible light communications (VLC) systems because of their quick response time [21]. Being incorporated with ultraviolet (UV) LEDs, the $CsPbBr_3$ PNCs have also been recently reported to function as detectors for VLC systems [22]. Because the visible light spectrum is 10,000 times larger than the radio frequency spectrum, VLC is regarded as an innovative technology that uses the principle of light modulation to facilitate high-speed data transmission, especially in enclosed spaces [23]. Mei *et al.* reported a packaged 80 × 80 μm c-plane blue μLED with a modulation bandwidth of 160 MHz [24]. VLC requires light sources that are not only efficient, but also with a high modulation bandwidth [25]. The modulation bandwidth is mainly determined by the carrier lifetime, and it varies depending on the LED configuration because LEDs grown on the c-plane exhibit longer recombination time due to the QCSE [19]. In contrast, LEDs grown on semipolar or nonpolar planes have faster radiative recombination because the QCSE is reduced [26,27]. The overlap of electron and hole wave functions in semipolar LEDs is stronger, allowing for faster radiative recombination and a higher modulation bandwidth. As a result, semipolar LEDs perform better in terms of bandwidth and exhibit a smaller wavelength shift, making them widely applicable for both high-speed VLC technology and high-resolution displays [28].

At present, there is a paucity of research on μLEDs that are suitable for both displays and VLC. In this study, we present a PNC–μLED device for a full-color display that is developed using a semipolar (20–21) blue μLED array with green-emitting $CsPbBr_3$ and red-emitting $CsPbBrI_2$ PNCs coated with SiO_2 to enhance the stability of the PNCs. The PNCs can successfully maintain the optical intensity after aging more than 1300 h. In addition, the semipolar (20–21) μLED array has a favorable wavelength-shift characteristic, which is only 2.7 nm compared to c-plane μLEDs with a similar multiple quantum well (MQW) design under different current densities. Moreover, the red and green colors created by the PNCs significantly improve the color purity as well as the color gamut, which can reach 127.23% of the NTSC and 95.00% of the Rec. 2020. Additionally, the proposed PNC–μLED device has the potential to be used for VLC applications, providing a maximum 3 dB bandwidth of 655 MHz and a data transmission rate of 1.2 Gb/s because of its short carrier lifetime. In general, the proposed PNC–μLED has a small color shift, large color gamut, high bandwidth, and strong stability of the SiO_2-coated PNC; thus, the device is a good prospect for use in display and VLC applications.

2. RESULTS

In this study, semipolar GaN was grown using an orientation-controlled epitaxy process on a patterned sapphire substrate (PSS). Details on the PSS and bulk GaN epitaxy can be found in our previous research [20]. In Fig. 1(a), the Xiamen University and National Chiao Tung University logos are visible, over which a 4-inch semipolar (20–21) LED epitaxial wafer and a 2-inch c-plane epitaxial wafer are placed. For both wafers, the high degree of transparency indicates their uniformity and low defect density. Large-area, low-cost epitaxial technology aims to improve the potential of semipolar LEDs for large-scale manufacturing. Figure 1(b) shows the SEM image of the LED epitaxial layer, with labels indicating the crystalline planes of GaN with a normal surface orientation toward (20–21) GaN. In a previous study, Ge doping was found to modify the N-polar (000–1) facet growth rate and decelerate the (101–1) growth rate, resulting in the removal of stacking faults produced in the (000–1) facets [29]. Relative to growth rates reported for c-plane epitaxy, these reported growth rates

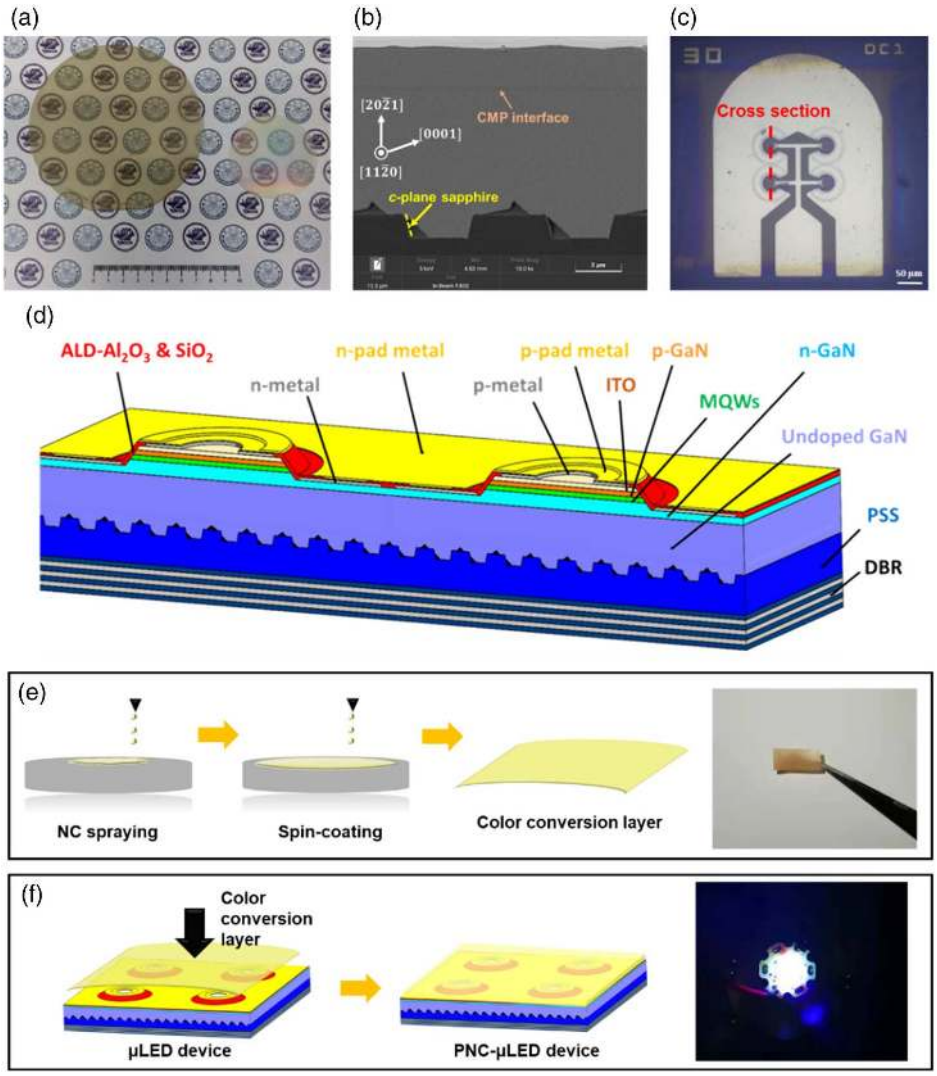

Fig. 1. (a) 4-inch semipolar (20–21) blue LED epitaxial wafer and 2-inch commercially available c-plane InGaN/GaN LED wafer with its rear side polished; (b) SEM image showing a cross-sectional view of the semipolar LED epitaxial wafer; (c) optical microscopic image of the 30 μm μLED array sample; schematic diagrams of (d) the semipolar (20–21) μLED structures, (e) the fabrication process and a photo of the color conversion layer, and (f) proposed PNC–μLED device.

imply that the crystallinity of the bulk GaN substrate is highly uniform.

The following processes were implemented to fabricate the μLEDs. First, we deposited a 200 nm thick layer of indium tin oxide (ITO) on top of the epitaxial structure of the LEDs. Then, we used a hydrochloric acid solution in conjunction with an inductively coupled plasma reactive ion etching (ICP–RIE) machine to etch a mesa with a depth of approximately 1 μm into the ITO layer. The μLED samples were annealed at 500°C for 2 min in pure nitrogen via a rapid thermal process to produce the optimized p-type ohmic contact. We used lithography and an electron gun, respectively, to pattern and deposit n-metal contacts, which consist of a Ti/Al/Ti/Au structure with a total thickness of 280 nm (comprising 20, 150, 10, and 100 nm layers, respectively). Moreover, atomic layer deposition (ALD)/plasma-enhanced chemical vapor deposition (PECVD) processes are used. A 30 nm thick aluminum oxide passivation layer was grown by trimethylaluminum and H_2O, with Ar purging at 300°C. Then, a 200 nm thick SiO_2 layer was grown by PECVD, with the holes fabricated via ICP–RIE. Finally, we deposited a Ni/Au composite structure as a p-metal, while a distributed Bragg reflector (DBR) was deposited on the rear surface of the wafer. An optical microscope image showing the sample in unilluminated state is shown in Fig. 1(c). The schematic cross-section of the μLED sample is shown in Fig. 1(d). To optimize high performance in VLC properties, we use ring-shaped electrodes to confine current injection, thus obtaining a higher current density. Second, we also deposited an ITO layer as the top contact layer on p-GaN, which can provide high current injection and reach a high modulation bandwidth. Additionally, we fabricated the PNC–SiO_2 color conversion layer for the backlight by mixing the red and green PNCs with the EVA polymer and spin-coating the mixture on glass substrates to form thin films. The fabrication detail can be

found in the Materials and Methods section. Figure 1(e) illustrates the fabrication detail and presents a photo of the as-fabricated films under natural light, which are composed of $CsPbBr_3$ – SiO_2 and $CsPbBrI_2$ – SiO_2. In Fig. 1(f), the color conversion layer is combined with the μLED, achieving the white-light PNC–μLED device for the backlight. This backlight solution is constructed under two considerations. The first is mass production; the film with mixed green and red PNCs is more feasible for manufacturing compared to the technique of printing the red and green PNCs above blue chips, respectively, to yield red and green pixels. The second is color homogeneity; the separated red and green pixels inevitably exhibit color differences among pixels, owing to the slight deviations in the thickness of the color conversion layer and/or densities of the PNCs. This can be effectively avoided using the unified color conversion layer.

For any fluorescent material, efficiency and stability are two key properties with equal importance. The former represents the instantaneous energy conversion rate, while the latter represents the longevity of the energy conversion efficiency. Based on our experience, $CsPbBr_3$ PNCs are intrinsically more stable than red-emitting $CsPbBrI_2$ PNCs, but have a lower PLQY under blue light excitation; on the other hand, iodine-containing red PNCs have a higher PLQY, but have decreased longevity against environmental factors. In practice, it is critical for every type of NC to achieve the best possible balance between PLQY and longevity. As mentioned earlier, the stability of NCs can be significantly enhanced by encapsulating them in a protective shell. Here, we used an all-inorganic SiO_2 shell, although this incurs with some loss to the PLQY. The all-inorganic material is crucial because it is unaffected by high-energy photons, such as blue light irradiation, which is ubiquitous in displays. For iodine-containing NCs, in particular, introducing the all-inorganic SiO_2 shell also facilitates crystallization during the fabrication process, as the pores inside the SiO_2 provide constraints on the growing NCs. In this study, the SiO_2 encapsulation was applied via a high-temperature sintering method. Before sintering, the mesopores in the molecular sieve (MS) absorb the precursors, such as CsI, CsBr, PbI_2, and $PbBr_2$. When the sintering temperature reaches 600°C, the mesoporous structures collapse and enclose the melted precursors inside the SiO_2 particles. During cooling, the perovskite forms inside the SiO_2, which constrains the PNCs inside that facilitate the formation of the crystal phase, thereby ensuring the high stability of the red-emitting PNCs. The PNC samples are referred to as $CsPbBr_3$ – SiO_2 and $CsPbBrI_2$ – SiO_2. The PNCs are sealed within solid SiO_2 particles and are thereby protected from the detrimental effects of oxygen and water vapor in the ambient environment. To compare the stability with traditional encapsulations, we also synthesized solution-processed PNCs for red and green using a traditional hot injection strategy (HIS) and ligand-assisted reprecipitation method (LARP), respectively. These solution-processed PNCs were embedded with ethylene vinyl acetate (EVA) and were denoted as $CsPbBrI_2$ – HIS and $CsPbBr_3$ – LARP, respectively.

The structural and surface characteristics of the SiO_2-coated PNCs were studied using X-ray diffraction (XRD), transmission electron microscopy (TEM), and energy dispersive X-ray spectroscopy (EDS). Figure 2 presents the XRD results for the $CsPbBrI_2$ – SiO_2 and $CsPbBr_3$ – SiO_2 samples. The characteristic peaks of perovskite emerge from the broad peak of the MCM-41 molecular sieve signal. The red line represents the XRD pattern of $CsPbBrI_2$ – SiO_2; because there is no standard PDF card for $CsPbBrI_2$, we provide the powder diffraction file of γ–$CsPbI_3$ as a reference. Relative to the peaks in the γ–$CsPbI_3$ pattern, the characteristic peaks are shifted slightly toward higher angles, which indicate the possible existence of $CsPbBrI_2$ – SiO_2. This is confirmed by the elementary mapping that will be described later. We also compared the characteristic peaks of $CsPbBr_3$ – SiO_2 with the standard ICSD#75-0421 card of cubic phase $CsPbBr_3$. The signals at 15°, 22°, 26°, 31°, 34°, 38°, and 44° were consistent, which confirms that PNCs were successfully crystallized in the sealed molecular sieve pores, thereby realizing SiO_2-coated PNCs.

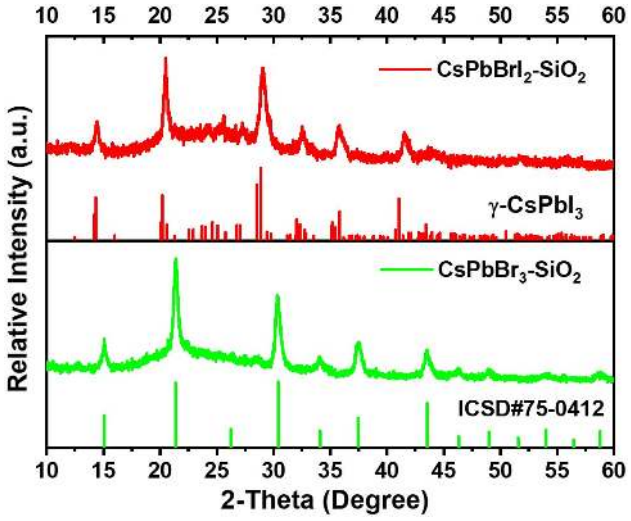

Fig. 2. XRD patterns of the $CsPbBrI_2$ – SiO_2 and $CsPbBr_3$ – SiO_2 PNCs.

The crystal morphology was shown using high-resolution TEM images at 800,000 magnification, and the specific lattice spacing was measured. Figures 3(a) and 3(c) show the TEM images of the $CsPbBr_3$ – SiO_2 and $CsPbBrI_2$ – SiO_2 PNCs, respectively. The fine structure of both PNC samples is also revealed from the EDS element maps, as illustrated in Fig. 4. These maps indicate that the spatial distribution of the elements within the PNCs is highly similar; they are confined to approximately circular regions surrounded by areas of SiO_2. This further confirms the encapsulation of the PNCs inside SiO_2 shells. The PNCs exhibit approximately spherical shapes and crystalline structures, which are in stark contrast with the amorphous SiO_2 that surrounds them. In Fig. 4(b), the distributions of Br and I overlap each other, confirming the formation of $CsPbBrI_2$. As shown in Fig. 3(b), the high-resolution TEM shows a lattice spacing of approximately 0.440 nm for the $CsPbBr_3$ – SiO_2 sample corresponding to the (110) lattice direction, which confirms the complete crystallization of $CsPbBr_3$. Although the theoretical lattice spacing of $CsPbBrI_2$ is unavailable due to the lack of a standard card, we still measured the observed lattice spacing at approximately 0.325 nm,

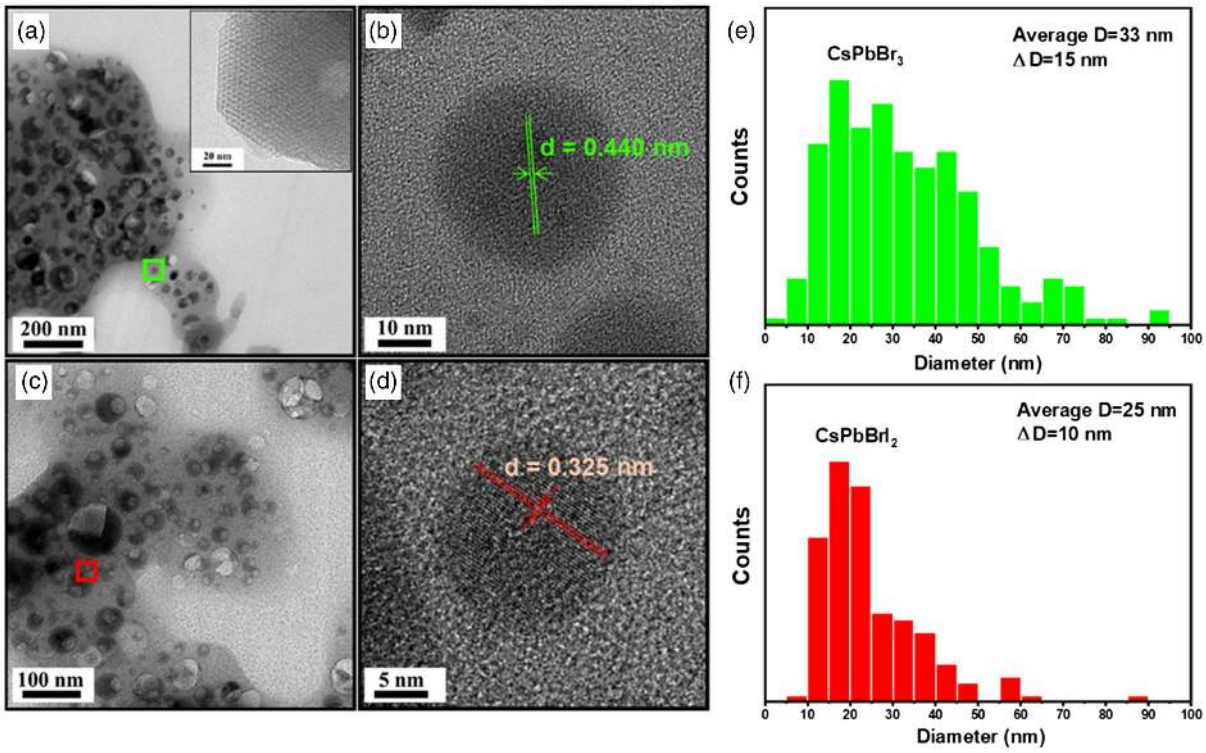

Fig. 3. TEM images of (a) $CsPbBr_3$ – SiO_2 and (c) $CsPbBrI_2$-C PNCs; high-resolution TEM images of the (b) $CsPbBr_3$ – SiO_2 and (d) $CsPbBrI_2$ – SiO_2 PNCs; and size distributions of (e) $CsPbBr_3$ and (f) $CsPbBr_2$. Inset in (a) is the TEM image of MS before sintering.

as shown in Fig. 3(d). This indicates that the synthesized $CsPbBrI_2$ – SiO_2 PNCs possess excellent crystallization. The size distributions of PNCs are illustrated in Figs. 3(e) and 3(f) for $CsPbBr_3$ and $CsPbBrI_2$, respectively, which indicate that the average sizes are 33 nm and 25 nm, respectively. Such a large size reveals that the quantum confinement effect can be neglected. We also post the TEM images of the empty MS before sintering, as illustrated in the inset of Fig. 3(a). In the TEM image, a periodic mesoporous structure can be clearly observed, which reveals that the pore size of MCM-41 is

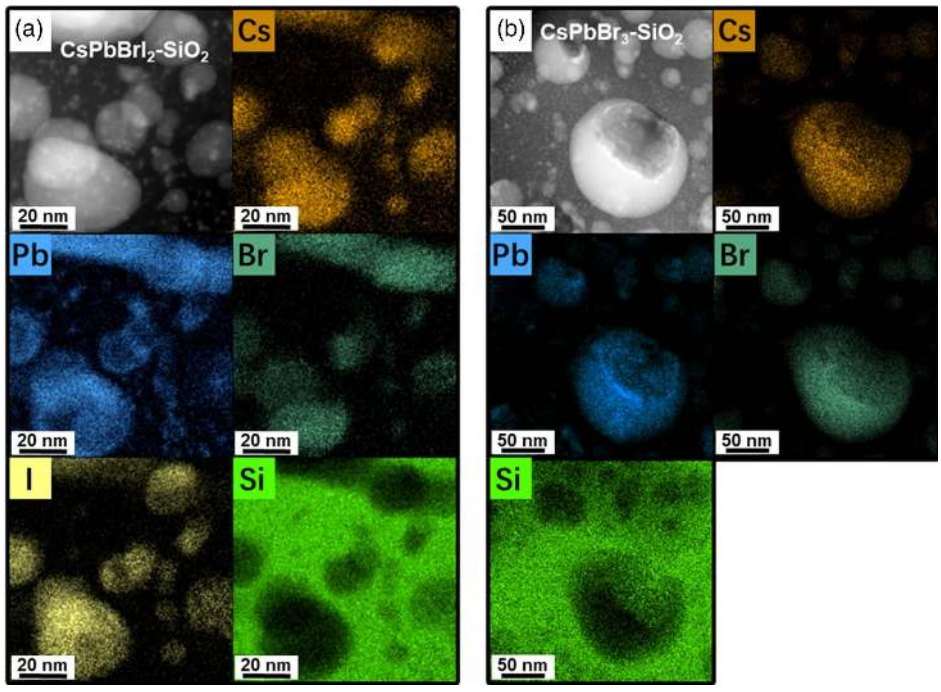

Fig. 4. EDS element maps of (a) $CsPbBrI_2$ – SiO_2 and (b) $CsPbBr_3$ – SiO_2 PNCs.

approximately 4.2 nm. Two questions have been raised. First, why are the sizes of the PNCs larger than that of the pore size? Second, why do the PNCs develop a spherical shape instead of cubic one, similar to those observed in solution-processed samples?

To answer these two questions, we may consider the formation of PNCs during the high-temperature sintering process. Before sintering, these pores are filled with precursor ions. When the sintering temperature reaches 600°C, the microstructure of MCM-41 collapses, whereby the mesoporous MSs are turned into solid SiO_2 particles, which seals the precursor ions inside. During cooling, the inner walls of the SiO_2 particles exert constrains on the precursor; the precursors inside simultaneously press the inner walls. This mutual pressure is isotropic, under which the precursor crystalizes into spherically shaped perovskite, whereas the inner spaces that contain the expanded perovskite crystals are reshaped into the same spherical shape. Therefore, in the TEM images of PNC-SiO_2, no periodic structures of the SiO_2 can be observed, which demonstrates that the original mesostructures of MS have been destroyed during the formation of NCs. The PNC is simultaneously formed in a spherical shape, owing to the isotropic constrains exerted by the SiO_2 particle sealing it. The study by Li *et al.* also provides a thorough discussion on the formation of PNCs inside SiO_2 MS [30].

The fabrication process is different from those also employing SiO_2 as encapsulations [31,32]. In these studies, the perovskite was synthesized in a solution, using an organic ligand as confinement, which is susceptible under UV illumination. In Wang's study, MS is employed, but only for the mechanical absorbing of the NCs inside its mesopores without closing the opening of the pores. This results in insufficient encapsulation; thus, the NC inside is still subjected to erosion.

Figures 5(a) and 5(b) display the absorption and PL spectra of the two types of PNC samples under UV excitation (365 nm). The PL emission wavelengths are 660 nm for $CsPbBrI_2$ – SiO_2 and 520 nm for $CsPbBr_3$ – SiO_2, with a narrow FWHM of 39 and 25 nm, respectively, implying high color purity. In addition, the narrow line emission widths of the PNCs suggest a wide color gamut of the PNC-based μLEDs. Figures 5(a) and 5(b) show the PNCs possess large absorption in the blue light region, indicating that the PNCs can absorb a certain amount of blue light from the μLED. Therefore, they are suitable for use as color converters in full-color displays. In addition, this overlap shows that there is a strong coupling between the excitons in the MQWs and the absorption dipoles of the PNCs [33]. The results for the longevities of the PNCs under ambient and blue irradiation are illustrated in Figs. 5(c) and 5(d), and the solution-processed samples exhibit faster degradation. For ambient aging, the L70 lifespans (the time at which the light intensity decreases to 70% of its initial value) of the solution-processed green $CsPbBrI_3$-LARP and red $CsPbBrI_2$-HIS PNCs are estimated to be 120 and 30 h, respectively, while the corresponding values for the blue light irradiation are 15 and 50 h, respectively. In stark contrast, the SiO_2-embedded samples exhibit remarkable stability, showing no degradation under identical aging conditions. These results confirm that encapsulating the PNCs within SiO_2 shells not only provides an enclosed environment that prevents exposure to water and oxygen, but also protects the PNCs from blue light radiation, which destroys traditional polymer shells.

Figure 6 illustrates the optical and electrical characteristics of the μLED array device. The current density-voltage (*J-V*) characteristics of the semipolar (20–21) blue μLED array with a chip diameter of 30 μm is shown in Fig. 6(a); the inset represents the optical image of the illuminated semipolar μLED

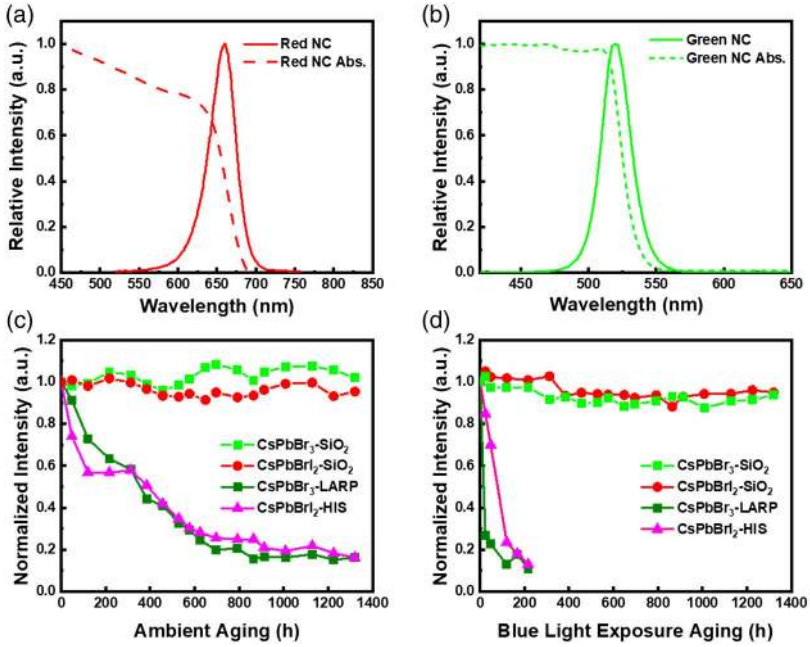

Fig. 5. UV-vis absorption and PL spectra of (a) $CsPbBrI_2$ – SiO_2 and (b) $CsPbBr_3$ – SiO_2. The PL properties of the red and green PNCs, as well as the solution-processed samples, are shown in response to (c) ambient and (d) blue light exposure.

array. The device has a forward turn-on voltage of 3.6 V with a maximum applied current density of 7076.4 A/cm^2, suggesting good material characteristics and high device performance. Figure 6(b) shows the electroluminescence (EL) spectra of the semipolar (20–21) blue μLED array for different injection currents, ranging from 2 to 200 mA. The EL spectrum shows a peak wavelength of 451.3 nm corresponding to an injection current of 200 mA with a slight blue shift as the current increases to 200 mA, which is attributed to the screening effect of QCSE due to increased free carriers and the band-filling effect of the localized energy states. The stability of the EL spectrum and the negligible wavelength shift in response to the increasing current are attributed to a reduction in the polarization-related electric field and the QCSE, indicating that these devices outperform their c-plane counterparts. This is due to the growth of MQWs on the semipolar facets of GaN. Figure 6(c) shows the wavelength peak and the FWHM shift in response to the increasing injection current density, where a negligible wavelength shift (only 2.7 nm) is observed. According to the stable EL spectrum, the FWHM is expected to decrease when the injection current decreases. However, the FWHM of the EL spectra increases from 22.02 to 23.42 nm, which is due to the band filling effect in the InGaN/GaN MQWs [34]. The dependence of the EQE on the injection current density and the emitted power of the semipolar μLED array are shown in Fig. 6(d). The emitted power continues to increase as the injection current increases. The peak efficiency corresponds to a low forward current density of 8.91 A/cm^2, followed by an efficiency droop of 69.0% as the injection current density increases to 7074 A/cm^2. This significant decline in efficiency is likely due to the device overheating. Further optimization of the chip fabrication process is expected to improve the efficiency droop problem.

In addition, the optical polarization characteristics of the semipolar μLED array, which are key features for display applications, are studied. Many studies report that semipolar or nonpolar μLEDs exhibit a high polarization ratio owing to their anisotropic polarized emission, which is an advantage compared with c-plane devices [35,36]. Figure 7(a) displays the maximum and minimum intensities of the polarized light emission from a semipolar array comprising four 30 μm μLEDs, with the result resembling a cosine function. The polarization ratio (P) can be calculated using

$$P = \frac{I_{\max} - I_{\min}}{I_{\max} + I_{\min}}, \tag{1}$$

where $I_{\max}$ and $I_{\min}$ are the maximum and minimum intensities of the polarized light transmitted by the polarizer, respectively. For the blue semipolar μLED array, P is determined to be 0.32, and this high polarization ratio is attributed to the separation of the top two valence bands caused by the anisotropic strain [28]. In the LCD, a polarizer is used to convert the light from the backlight into polarized light, causing a larger power loss. Owing to this polarization ratio of 0.32, when the light of the semipolar μLED passes through the polarizer, the transmittance becomes 66%, which exceeds the value of 50% of the natural light. Furthermore, the semipolar μLED can be implemented by polarization-division multiplexing to enhance the rate of data transmission and add another degree of freedom that can amplify the transmission capacity. According

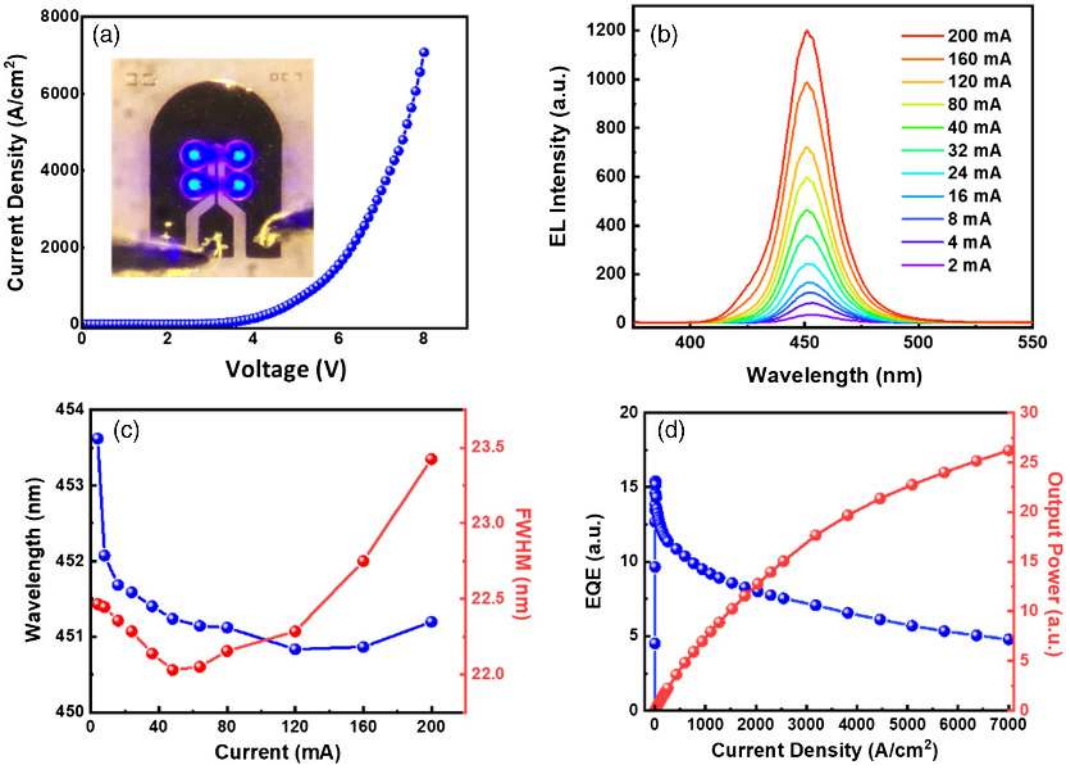

Fig. 6. (a) Current density–voltage (J–V) curve for the 30 μm μLED array and its illuminated image; (b) EL spectra for different injection currents; (c) peak wavelength shift and FWHM as a function of current density; and (d) EQE and emitted power as a function of current density.

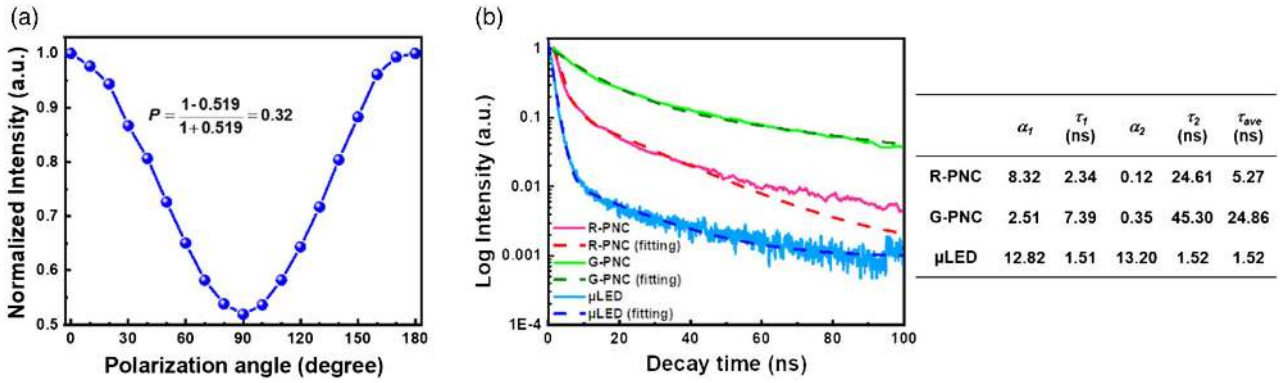

	α_1	τ_1 (ns)	α_2	τ_2 (ns)	τ_{ave} (ns)
R-PNC	8.32	2.34	0.12	24.61	5.27
G-PNC	2.51	7.39	0.35	45.30	24.86
μLED	12.82	1.51	13.20	1.52	1.52

Fig. 7. (a) Polarization characteristics of the 30 μm × 4 semipolar μLED array; and (b) TRPL curves for the semipolar μLED array and the PNCs.

to this polarization ratio, a high modulation bandwidth is expected for this semipolar blue μLED array. Figure 7(b) shows the time-resolved photoluminescence (TRPL) measurements of the semipolar blue μLED array, red-emitting PNCs, and green-emitting PNCs with PL peaks at 450, 650, and 508 nm, respectively. The PNCs were excited using a 450 nm laser, while the blue μLED array was excited using a 365 nm UV source. The normalized TRPL trace is given as

$$I(t) = \alpha_1 \exp\left(-\frac{t}{\tau_1}\right) + \alpha_2 \exp\left(-\frac{t}{\tau_2}\right), \tag{2}$$

where $I(t)$ is the luminous intensity, τ_1 and τ_2 represent the radiation decay time under different mechanisms, and α_1 and α_2 represent the radiation attenuation ratio under different mechanisms. The specific values of these parameters are reflected in Fig. 7(b). According to

$$\tau_{\text{ave}} = \frac{\alpha_1\tau_1 + \alpha_2\tau_2}{\alpha_1 + \alpha_2}, \tag{3}$$

the average lifetimes τ_{ave} were found to be 1.52, 24.86, and 5.27 ns for the semipolar blue μLED array, green PNCs, and red PNCs, respectively. It was found that the minority carrier lifetime of the semipolar device is extraordinarily short; this is attributed to the less-polarized electric field, which results in greater overlap of the electron-hole wave function. In addition, this shorter lifetime will lead to a faster carrier recombination and a higher modulation bandwidth for the semipolar device. Further, the carriers are distributed more uniformly in the active region of semipolar μLEDs owing to the rectangular-shaped barrier, which enables carriers to have a faster transport mechanism.

Next, the VLC performance of the PNC–μLED was studied, as shown in Fig. 8. The modulation bandwidth

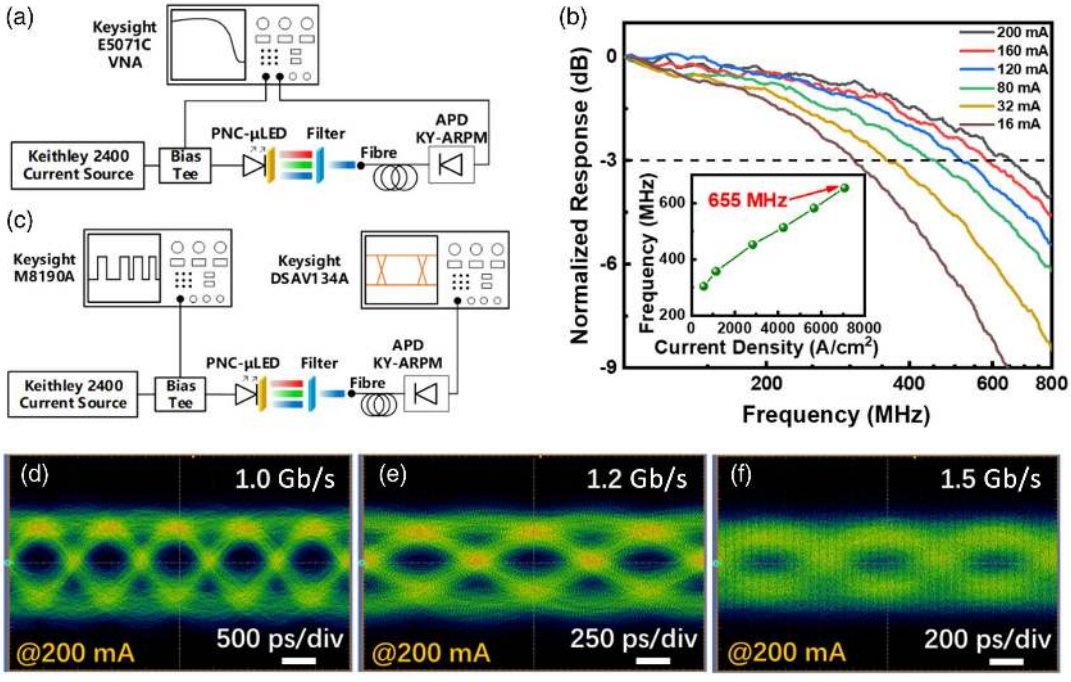

Fig. 8. (a) Schematic diagram for bandwidth measurement; (b) frequency response for the PNC–μLED; (c) schematic diagram for the eye diagram measurement; (d)–(f) eye diagrams of the PNC–μLED at 1.0, 1.2, and 1.5 Gb/s, respectively.

measurement was performed using a vector network analyzer (VNA; Keysight E5071C). As shown in Fig. 8(a), a bias tee (11612A, 45 MHz–26.5 GHz) combines AC signals from the VNA with DC signals from the current source and applies it to the PNC–μLED, which was probed by a high-speed microprobe (ACP40-GS-250, DC–40 GHz). The PNC bandwidth is approximately tens of MHz, which is considerably lower than that of the μLED. Therefore, a filter is used to remove the red and green light generated by PNCs in the experiment [27]. The blue light passing through the filter was collected using an optical fiber, which was coupled with an avalanche photodiode (APD) (SPA-3, DC–2 GHz). The converted signal was traced back to the VNA, where the modulation bandwidth was measured. Figure 8(b) shows the frequency response of the PNC–μLED, revealing that the 3 dB bandwidth increases, owing to the higher injected carrier density in the active region as the injection current increases. This results in a built-in electric field and decreased carrier lifetime. The highest 3 dB bandwidth was measured as 655 MHz, corresponding to an injection current of 200 mA (current density of 7074 A/cm^2). This is quite promising for VLC applications, as shown in the inset of Fig. 8(b). The proportionality of the 3 dB bandwidth in response to an increase in the current implies that the 3 dB bandwidth is not limited by the RC delay. Therefore, the modulation bandwidth is not influenced by the RC time constant, but by the recombination lifetime. In Fig. 8(c), the Keysight M8190A produced the back-to-back non-return-to-zero on-off key (NRZ-OOK) $2^7 - 1$ pseudorandom bit sequence (PRBS-7), and the Keysight DSAV134A oscilloscope reported the eye diagram results. The eye diagrams of the PNC–μLED were clear and open at 1.0 and 1.2 Gb/s, as shown in Figs. 8(d)–9(f), owing to the sufficiently high value of the 3 dB bandwidth. However, due to a comparatively poor SNR, the eye becomes unclear when the data rate approaches 1.5 Gb/s, although using high-level modulation techniques is supposed to achieve a higher data rate.

Figure 9 presents the performance of the PNC–μLED for the display backlight application under different current densities between 2.55 and 203.83 A/cm^2. Because of its narrow EL spectrum, the RGB pixel assembled from the semipolar μLEDs and PNCs exhibited a wide color gamut of 127.23% of the NTSC and 95.00% of the Rec. 2020. The PNC–μLED device fabricated in this study using a semipolar μLED array with red and green PNCs showed significant color stability and wide color-gamut characteristics, demonstrating tremendous potential for display backlight applications.

Therefore, the device proposed in this study could be used for display applications when operated at low current densities, while at high current densities it could be used for VLC applications. If the device is required for display and communications simultaneously, for the safety of the user's eyes, the device should work at the low current density region, which is below 200 A/cm^2. In this case, the μLED bandwidth may not reach the highest value, but it can still reach approximately 245 MHz at 203.83 A/cm^2, which is sufficient for normal communications scenarios. Moreover, compared to conventional c-plane μLEDs, the semipolar μLED array proposed here not only reduces the color shift at different current densities but also increases the rate of carrier recombination, thereby increasing the modulation bandwidth for VLC applications. The SiO_2-coated PNCs proposed in this study possess greatly enhanced stability and can achieve a wide color gamut for display applications.

3. DISCUSSION

Highly stable PNCs were manufactured with a SiO_2 coating, exhibiting high PL performance and high color purity due to their narrow FWHM. The semipolar μLED array exhibits great potential for display-related and VLC applications, as exemplified by its negligible wavelength shift, high polarization properties, and peak 3 dB bandwidth of 655 MHz under an injection current density of 200 mA. A full-color display, fabricated using the semipolar μLED array with PNCs, exhibited high color stability and wide color-gamut features, achieving 127.23% of the NTSC and 95.00% of the Rec. 2020 on the CIE 1931. The Cs

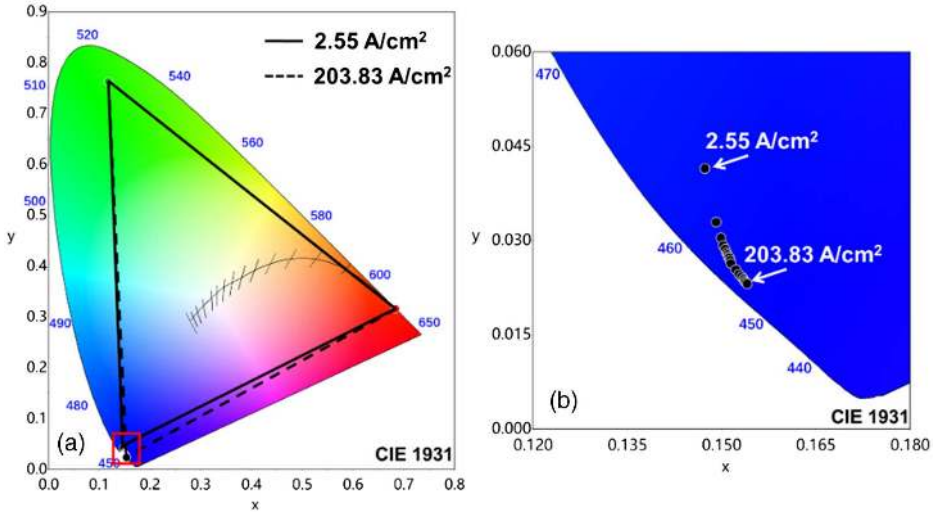

Fig. 9. (a) Color gamut of the PNC–μLED under different current densities; and (b) color shift of blue semipolar μLEDs under different current densities.

and Pb in the PNC-SiO_2 samples may raise concerns on environmental issues. In our opinion, the solid sealing of SiO_2 will prevent the leakage of these poisonous elements, which will lower the potential environmental hazards. These characteristics demonstrate tremendous potential for such PNC-μLED devices to be used for full-color displays and in VLC applications.

4. MATERIALS AND METHODS

A. Synthesis of $CsPbBrI_2$ – SiO_2 and $CsPbBr_3$ – SiO_2 PNCs

A precursor solution was prepared by mixing a particular amount of precursor salts with MCM-41 molecular sieve (masses are listed in Table 1) and dispersing this mixture in 25 mL of purified water. Next, the precursor solution was subjected to ultrasonic vibration for 20 min and stirred vigorously for 10 min to improve dispersion. The precursor solution was transferred to a crucible and placed in a tube furnace filled with high purity Ar gas. The temperature of the tube furnace was first raised to 200°C, and it was maintained for 1 h to evaporate the water. Then, continuous sintering was performed at a temperature of 750°C for 30 min with an Ar flow rate of 15 mL/min. Subsequently, the samples were cooled to room temperature under Ar protection, during which their colors gradually changed, finally crystallizing into PNCs. The final $CsPbBrI_2$ – SiO_2 was immersed in purified water and subjected to a second ultrasonic vibration, then washed and filtered by suction, and dried in a vacuum evaporator at 40°C.

B. Synthesis of PNC $CsPbBr_3$-LARP

We followed a typical ligand-assisted reprecipitation method (LARP). We mixed CsBr (0.2 mmol) with $PbBr_2$ (0.4 mmol) and added the mixture to a DMF (5 mL) solution, which was stirred magnetically for 4 h until the precursor mixture was completely dissolved. Next, butyric acid (BA, 300 μL) and oleylamine (OAm, 160 μL) were added as the ligand for the precursor solution. Simultaneously, we dissolved 0.5 g of EVA in 5 mL of toluene. Then, 200 μL of the precursor solution was added dropwise to the EVA-toluene mixture and stirred vigorously. Finally, after the gradual volatilization of the toluene, we obtained $CsPbBr_3$ PNCs embedded in EVA composite films. This sample is hereafter referred to as PNC $CsPbBr_3$-LARP.

C. Synthesis of PNC $CsPbBrI_2$-HIS

This sample was fabricated using the traditional hot injection strategy (HIS) in a two-step process.

Step I: Preparation of Cs-oleate precursor. 0.407 g of Cs_2CO_3, 1.25 mL of oleic acid, and 20 mL of 1-octadecene (ODE) were accurately weighed and mixed in a 100 mL three-necked flask. The mixture was heated to 120°C in vacuum for 1 h to remove water and oxygen. Then, the temperature was increased to 150°C in a N_2 environment and maintained for 10 min until the Cs_2CO_3 was completely dissolved. The Cs-oleate precursor solution was stored in a refrigerator and maintained at 100°C before use for the syntheses of PNCs.

Step II: Synthesis of PNC $CsPbBrI_2$-HIS. In this procedure, 0.0918 g of $PbBr_2$, 0.2305 g of PbI_2, 20 mL of ODE, 2.6 mL of oleic acid, and 2.6 mL of OAm were mixed in a 100 mL three-necked flask. Water and oxygen were removed under vacuum conditions for 30 min at 120°C. Next, the temperature was increased to 180°C under flowing N_2 and maintained for 10 min. Subsequently, 1.6 mL of Cs-oleate precursor, which was pre-heated at 100 °C, was injected rapidly into the Pb-oleate solution. After approximately 5 s, the three-necked flask was placed in an ice bath and cooled to room temperature. Then, the crude solution was centrifuged at 8000 r/min for 5 min. Finally, the supernatant was discarded, and the precipitate was dispersed in toluene. The final sample is hereafter referred to as PNC $CsPbBrI_2$-HIS.

Table 1. Precursor Masses

Samples	CsBr (g)	PbI_2 (g)	$PbBr_2$ (g)	MCM-41 (all-silica) MS (g)
$CsPbBrI_2$ – SiO_2	0.73	1.59	0	2.00
$CsPbBr_3$ – SiO_2	0.73	0	1.27	2.00

D. Fabrication of PNC-SiO_2 Color Conversion Films

In this process, 0.03 g of $CsPbBrI_2$ – SiO_2 and 0.03 g $CsPbBr_3$ – SiO_2 were mixed with 10 mL toluene, and the mixture underwent supersonic vibration for 10 min. Some EVA was dissolved into the mixture, and it was heated to 50°C while stirring for 30 min. The mixture was then spin-coated (1800 rad/s) on a glass substrate to obtain films with homogeneous thickness. The film was excited by a blue LED under a driving current of 50 mA.

Characterization of PL and absorption: The PL was measured by a spectrometer (F-7000, Hitachi, Ltd., Tokyo, Japan) under excitation of a 450 nm blue light source; the absorption spectra were measured by a UV-2550 (Shimadzu, Kyoto, Japan).
Characterization of XRD: A SmartLab SE (Rigaku, Tokyo, Japan) instrument was used to perform the XRD measurements of the samples for a 2θ range from 10° to 60°.
Characterization of TEM and EDS: TEM images were acquired using a JEM 2100 (JEOL Ltd., Tokyo, Japan) and a Talos F200X (Thermo Fisher Scientific, Waltham, MA, USA). The samples were prepared using a focused ion beam by a Helios 660 (Thermo Fisher Scientific). The EDS elementary mapping images were acquired using the Talos F200X built-in camera.
Characterization of TRPL: The TRPLs were tested by an FLS-980 series of fluorescence spectrometers (Edinburgh Instruments, Livingston, Scotland, UK). The excited source of NC was a 450 nm blue laser, and we selected a 365 nm UV source as the excitation light source for our blue μLED.
Aging test: To test the durability of the fabricated PNCs, an ambient storage and a blue light illumination test were carried out. The ambient storage test was conducted with approximately 70% relative humidity at 25°C without direct light illumination. For the blue LED illumination test, 450 nm LEDs (powered by a 50 mA DC current) were employed as the blue light sources. The test was performed at room temperature and the average distance between the blue LED chip and sample was 1 cm. For both ambient and blue light illumination tests, the PL spectra of the samples were measured under the excitation of 356 nm LEDs at certain intervals using a spectrometer

(Spectro 320, Instrument Systems Optische Messtechnik GmbH, Munich, Germany).

Funding. National Natural Science Foundation of China (11904302, 61504112); Major Project of the Science and Technology in Fujian Province of China (2019HZ020013); Industry University Cooperation Project of Science and Technology Department in Fujian Province of China (2018H6022); Major Science and Technology Projects in Xiamen of China (3502Z20191015); Fundamental Research Funds for the Central Universities (20720190005).

Acknowledgment. The authors thank Prof. Rong Zhang and Prof. Rongjun Xie of Xiamen University, Prof. Jung Han of Yale University, Prof. Chi-Wai Chow of Taiwan Chiao Tung University, and Prof. Gong-Ru Lin of Taiwan University for their advice and technical support. We also appreciate the contributions to experimental work, manuscript editing, and constructive discussions from Guolong Chen, Zeping Wang, Zhibin Shangguan, Weizhi Huang, Youcai Deng, Xiaotong Fan, and Xiao Yang of the Solid-state Lighting Laboratory, Xiamen University.

Disclosures. The authors declare no conflicts of interest.

Data Availability. Data underlying the results presented in this paper are not publicly available at this time but may be obtained from the authors upon reasonable request.

†These authors contributed equally to this paper.

REFERENCES

1. C. Chang, K. Bang, G. Wetzstein, B. Lee, and L. Gao, "Toward the next-generation VR/AR optics: a review of holographic near-eye displays from a human-centric perspective," Optica **7**, 1563–1578 (2020).
2. Y.-M. Huang, K. J. Singh, A.-C. Liu, C.-C. Lin, Z. Chen, K. Wang, Y. Lin, Z. Liu, T. Wu, and H.-C. Kuo, "Advances in quantum-dot-based displays," Nanomaterials **10**, 1327 (2020).
3. T. Wu, C.-W. Sher, Y. Lin, C.-F. Lee, S. Liang, Y. Lu, S.-W. H. Chen, W. Guo, H.-C. Kuo, and Z. Chen, "Mini-LED and micro-LED: promising candidates for the next generation display technology," Appl. Sci. **8**, 1557 (2018).
4. S.-W. Huang Chen, C.-C. Shen, T. Wu, Z.-Y. Liao, L.-F. Chen, J.-R. Zhou, C.-F. Lee, C.-H. Lin, C.-C. Lin, C.-W. Sher, P.-T. Lee, A.-J. Tzou, Z. Chen, and H.-C. Kuo, "Full-color monolithic hybrid quantum dot nanoring micro light-emitting diodes with improved efficiency using atomic layer deposition and nonradiative resonant energy transfer," Photon. Res. **7**, 416–422 (2019).
5. Y. Huang, E.-L. Hsiang, M.-Y. Deng, and S.-T. Wu, "Mini-LED, micro-LED and OLED displays: present status and future perspectives," Light Sci. Appl. **9**, 105 (2020).
6. J. Cho, J. H. Park, J. K. Kim, and E. F. Schubert, "White light-emitting diodes: history, progress, and future," Laser Photon. Rev. **11**, 1600147 (2017).
7. D. Hwang, A. Mughal, C. Pynn, S. Nakamura, and S. Denbaars, "Sustained high external quantum efficiency in ultrasmall blue III-nitride micro-LEDs," Appl. Phys. Express **10**, 032101 (2017).
8. X. Wang, Z. Bao, Y.-C. Chang, and R.-S. Liu, "Perovskite quantum dots for application in high color gamut backlighting display of light-emitting diodes," ACS Energy Lett. **5**, 3374–3396 (2020).
9. C.-H. Lin, A. Verma, C.-Y. Kang, Y.-M. Pai, T.-Y. Chen, J.-J. Yang, C.-W. Sher, Y.-Z. Yang, P.-T. Lee, C.-C. Lin, Y.-C. Wu, S. K. Sharma, T. Wu, S.-R. Chung, and H.-C. Kuo, "Hybrid-type white LEDs based on inorganic halide perovskite QDs: candidates for wide color gamut display backlights," Photon. Res. **7**, 579–585 (2019).
10. C. C. Lin and R.-S. Liu, "Advances in phosphors for light-emitting diodes," J. Phys. Chem. Lett. **2**, 1268–1277 (2011).
11. Z. Liu, C.-H. Lin, B.-R. Hyun, C.-W. Sher, Z. Lv, B. Luo, F. Jiang, T. Wu, C.-H. Ho, H.-C. Kuo, and J.-H. He, "Micro-light-emitting diodes with quantum dots in display technology," Light Sci. Appl. **9**, 83 (2020).
12. J. A. Steele, H. Jin, I. Dovgaliuk, R. F. Berger, T. Braeckevelt, H. Yuan, C. Martin, E. Solano, K. Lejaeghere, S. M. J. Rogge, C. Notebaert, W. Vandezande, K. P. F. Janssen, B. Goderis, E. Debroye, Y.-K. Wang, Y. Dong, D. Ma, M. Saidaminov, H. Tan, Z. Lu, V. Dyadkin, D. Chernyshov, V. Van Speybroeck, E. H. Sargent, J. Hofkens, and M. B. J. Roeffaers, "Thermal unequilibrium of strained black CsPbI3 thin films," Science **365**, 679–684 (2019).
13. S. Masi, A. F. Gualdrón-Reyes, and I. Mora-Seró, "Stabilization of black perovskite phase in $FAPbI_3$ and $CsPbI_3$," ACS Energy Lett. **5**, 1974–1985 (2020).
14. Y. Wei, Z. Cheng, and J. Lin, "An overview on enhancing the stability of lead halide perovskite quantum dots and their applications in phosphor-converted LEDs," Chem. Soc. Rev. **48**, 310–350 (2019).
15. Z. Shangguan, X. Zheng, J. Zhang, W. Lin, W. Guo, C. Li, T. Wu, Y. Lin, and Z. Chen, "The stability of metal halide perovskite nanocrystals–a key issue for the application on quantum-dot-based micro light-emitting diodes display," Nanomaterials **10**, 1375 (2020).
16. L. Shi, L. Meng, F. Jiang, Y. Ge, F. Li, X. G. Wu, and H. Zhong, "*In situ* inkjet printing strategy for fabricating perovskite quantum dot patterns," Adv. Funct. Mater. **29**, 1903648 (2019).
17. M. C. C. d. Oliveira, A. S. A. C. Diniz, M. M. Viana, and V. d. F. C. Lins, "The causes and effects of degradation of encapsulant ethylene vinyl acetate copolymer (EVA) in crystalline silicon photovoltaic modules: a review," Renew. Sustain. Energy Rev. **81**, 2299–2317 (2018).
18. T. Takeuchi, S. Sota, M. Katsuragawa, M. Komori, H. Takeuchi, H. Amano, and I. Akasaki, "Quantum-confined stark effect due to piezoelectric fields in GaInN strained quantum wells," Jpn. J. Appl. Phys. **36**, L382–L385 (1997).
19. S.-W. H. Chen, Y.-M. Huang, Y.-H. Chang, Y. Lin, F.-J. Liou, Y.-C. Hsu, J. Song, J. Choi, C.-W. Chow, C.-C. Lin, R.-H. Horng, Z. Chen, J. Han, T. Wu, and H.-C. Kuo, "High-bandwidth green semipolar (20-21) InGaN/GaN micro light-emitting diodes for visible light communication," ACS Photon. **7**, 2228–2235 (2020).
20. S.-W. H. Chen, Y.-M. Huang, K. J. Singh, Y.-C. Hsu, F.-J. Liou, J. Song, J. Choi, P.-T. Lee, C.-C. Lin, Z. Chen, J. Han, T. Wu, and H.-C. Kuo, "Full-color micro-LED display with high color stability using semipolar (20-21) InGaN LED and quantum-dot photoresist," Photon. Res. **8**, 630–636 (2020).
21. K. James Singh, Y.-M. Huang, T. Ahmed, A.-C. Liu, S.-W. Huang Chen, F.-J. Liou, T. Wu, C.-C. Lin, C.-W. Chow, G.-R. Lin, and H.-C. Kuo, "Micro-LED as a promising candidate for high-speed visible light communication," Appl. Sci. **10**, 7384 (2020).
22. C. H. Kang, I. Dursun, G. Liu, L. Sinatra, X. Sun, M. Kong, J. Pan, P. Maity, E.-N. Ooi, T. K. Ng, O. F. Mohammed, O. M. Bakr, and B. S. Ooi, "High-speed colour-converting photodetector with all-inorganic $CsPbBr_3$ perovskite nanocrystals for ultraviolet light communication," Light Sci. Appl. **8**, 94 (2019).
23. S. Zhang, D. Tsonev, S. Videv, S. Ghosh, G. A. Turnbull, I. D. W. Samuel, and H. Haas, "Organic solar cells as high-speed data detectors for visible light communication," Optica **2**, 607–610 (2015).
24. S. Mei, X. Liu, W. Zhang, R. Liu, L. Zheng, R. Guo, and P. Tian, "High-bandwidth white-light system combining a micro-LED with perovskite quantum dots for visible light communication," ACS Appl. Mater. Interfaces **10**, 5641–5648 (2018).
25. P. Tian, X. Liu, S. Yi, Y. Huang, S. Zhang, X. Zhou, L. Hu, L. Zheng, and R. Liu, "High-speed underwater optical wireless communication using a blue GaN-based micro-LED," Opt. Express **25**, 1193–1201 (2017).
26. G. Kozlowski, S. Schulz, and B. Corbett, "Polarization matching design of InGaN-based semi-polar quantum wells—a case study of (11–22) orientation," Appl. Phys. Lett. **104**, 051128 (2014).
27. D. Rosales, B. Gil, T. Bretagnon, B. Guizal, F. Zhang, S. Okur, M. Monavarian, N. Izyumskaya, V. Avrutin, Ü. Özgür, H. Morkoç, and J. H. Leach, "Excitonic recombination dynamics in non-polar GaN/AlGaN quantum wells," J. Appl. Phys. **115**, 073510 (2014).

28. H. Zhang, P. Li, H. Li, J. Song, S. Nakamura, and S. P. Denbaars, "High polarization and fast modulation speed of dual wavelengths electroluminescence from semipolar (20-21) micro light-emitting diodes with indium tin oxide surface grating," Appl. Phys. Lett. **117**, 181105 (2020).
29. J. Song, J. Choi, C. Zhang, Z. Deng, Y. Xie, and J. Han, "Elimination of stacking faults in semipolar GaN and light-emitting diodes grown on sapphire," ACS Appl. Mater. Interfaces **11**, 33140–33146 (2019).
30. Q. Zhang, B. Wang, W. Zheng, L. Kong, Q. Wan, C. Zhang, Z. Li, X. Cao, M. Liu, and L. Li, "Ceramic-like stable CsPbBr3 nanocrystals encapsulated in silica derived from molecular sieve templates," Nat. Commun. **11**, 31 (2020).
31. C. Sun, Y. Zhang, C. Ruan, C. Yin, X. Wang, Y. Wang, and W. W. Yu, "Efficient and stable white LEDs with silica-coated inorganic perovskite quantum dots," Adv. Mater. **28**, 10088–10094 (2016).
32. H.-C. Wang, S.-Y. Lin, A.-C. Tang, B. P. Singh, H.-C. Tong, C.-Y. Chen, Y.-C. Lee, T.-L. Tsai, and R.-S. Liu, "Mesoporous silica particles integrated with all-inorganic $CsPbBr_3$ perovskite quantum-dot nanocomposites (MP-PQDs) with high stability and wide color gamut used for backlight display," Angew. Chem. **55**, 7924–7929 (2016).
33. M. Achermann, M. A. Petruska, S. Kos, D. L. Smith, D. D. Koleske, and V. I. Klimov, "Energy-transfer pumping of semiconductor nanocrystals using an epitaxial quantum well," Nature **429**, 642–646 (2004).
34. I.-K. Park, M.-K. Kwon, S.-B. Seo, J.-Y. Kim, J.-H. Lim, and S.-J. Park, "Ultraviolet light-emitting diodes with self-assembled InGaN quantum dots," Appl. Phys. Lett. **90**, 111116 (2007).
35. S. E. Brinkley, Y.-D. Lin, A. Chakraborty, N. Pfaff, D. Cohen, J. S. Speck, S. Nakamura, and S. P. DenBaars, "Polarized spontaneous emission from blue-green m-plane GaN-based light emitting diodes," Appl. Phys. Lett. **98**, 011110 (2011).
36. Y. Zhao, S. Tanaka, Q. Yan, C.-Y. Huang, R. B. Chung, C.-C. Pan, K. Fujito, D. Feezell, C. G. V. d. Walle, J. S. Speck, S. P. DenBaars, and S. Nakamura, "High optical polarization ratio from semipolar (20-2-1) blue-green InGaN/GaN light-emitting diodes," Appl. Phys. Lett. **99**, 051109 (2011).